ARTICLE

Molecular Structure of Single-Stranded DNA on the ZnS Surface of Quantum Dots

Xingfei Wei, Chi Chen, Yinong Zhao, Ewa Harazinska, Mark Bathe, and Rigoberto Hernandez*

Cite This: ACS Nano 2022, 16, 6666−6675 | Read Online

ACCESS | Metrics & More | Article Recommendations | Supporting Information

ABSTRACT: DNA-based nanoparticle assemblies have emerged as leading candidates in the development of bioimaging materials, photonic devices, and computing materials. Here, we combine atomistic simulations and experiments to characterize the wrapping mechanism of chimeric single-stranded DNA (ssDNA) on CdSe-ZnS (core−shell) quantum dots (QDs) at different ratios of the phosphorothioate (PS) modification of the bases. We use an implicit solvent, all-atom ssDNA model to match the experimentally calculated ssDNA conformation at low salt concentrations. Through simulation, we find that 3-mercaptopropionic acid (MPA) induces electrostatic repulsion and O-(2-mercaptoethyl)-O-methyl-hexa (ethylene glycol) (mPEG) induces steric exclusion, and both reduce the binding affinity of ssDNA. In both simulation and experiment, we find that ssDNA is closer to the QD surface when the QD size is larger. The effect of the PS-base ratio on the conformation of ssDNA is also elaborated in this work. We found through MD simulations, and confirmed by transmission electron microscopy, that the maximum valence numbers are 1, 2, and 3 on QDs of 6, 9, and 14 nm in diameter, respectively. We conclude that the maximum ssDNA valence number is linearly related to the QD size, $n \propto R$, and justify this finding through an electrostatic repulsion mechanism.

KEYWORDS: ssDNA wrapping, conformation, ZnS QD, NP assembly, FRET
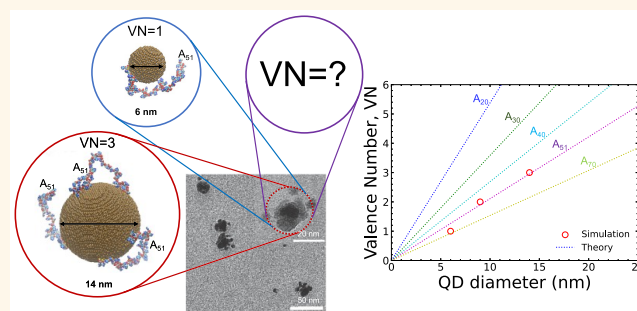
INTRODUCTION

DNA linked nanoparticle (NP) assemblies have been used in various applications, such as biological delivery, bioimaging, programmable materials, photonics, electronics, and computing devices.[1−10] DNA linked gold nanoparticle (AuNP) core−satellite superstructures have been reported to reduce NP retention and improve NP *in vivo* tumor accumulation and whole-body elimination.[11] Using DNA icosahedron-encapsulated QDs, Bhatia et al.[12] demonstrated real-time imaging of three different endocytic ligands in live cells. As early as 2009, DNA wrapped CdSe/ZnS QDs were seen to achieve simple logic gate operations.[13] More recently, Kim et al.[14] developed a molecular computing platform using DNA strands as the software and NPs as the hardware, performing tasks such as data storage and computing. Indeed, a variety of DNA linked NP nanoarchitectures have been fabricated based on DNA scaffolds[15] or DNA origami frames.[4,16,17]

Nevertheless, the structure of a single-stranded DNA (ssDNA) wrapped on a NP surface remains unclear. Achieving a precise QD-ssDNA assembly also remains a challenge. Recently, Fan and co-workers[18] demonstrated that ssDNA wrapped AuNPs and ssDNA wrapped QDs can make programmable atom-like NPs that can further perform Boolean

logic operations. Devices relying on ssDNA wrapped AuNPs of different lengths have been fabricated as nanothermometers,[19] taking advantage of the fact that the melting temperature of DNA is related to the chain length.[19] A variety of DNA linked QD biosensors have also been developed relying on the fact that the Förster Resonance Energy Transfer (FRET) efficiency of QDs depends on the NP size, distance (QD to AuNP and QD to QD) and connectivity.[20−23] Precise engineering of the valence position and valence number of an NP is thus critical to developing functional NP assemblies. Determining the mechanism of DNA wrapping on a NP or QD is also crucial for emerging DNA-based materials design.
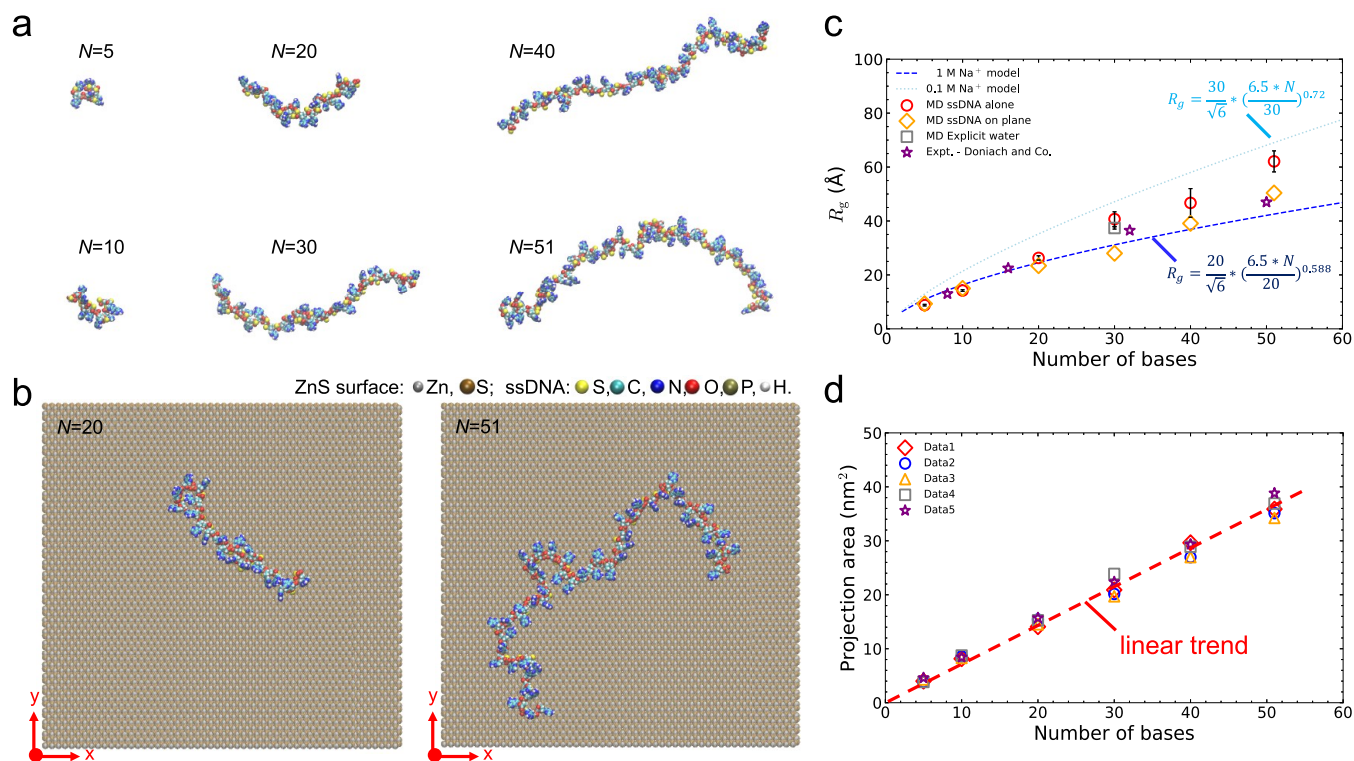
In 2013, Farlow et al.[24] introduced a method taking advantage of the steric exclusion effect to synthesize monovalent ssDNA wrapped QD with high yield for cell imaging. Yao et al.[18] achieved multiple binding spots on
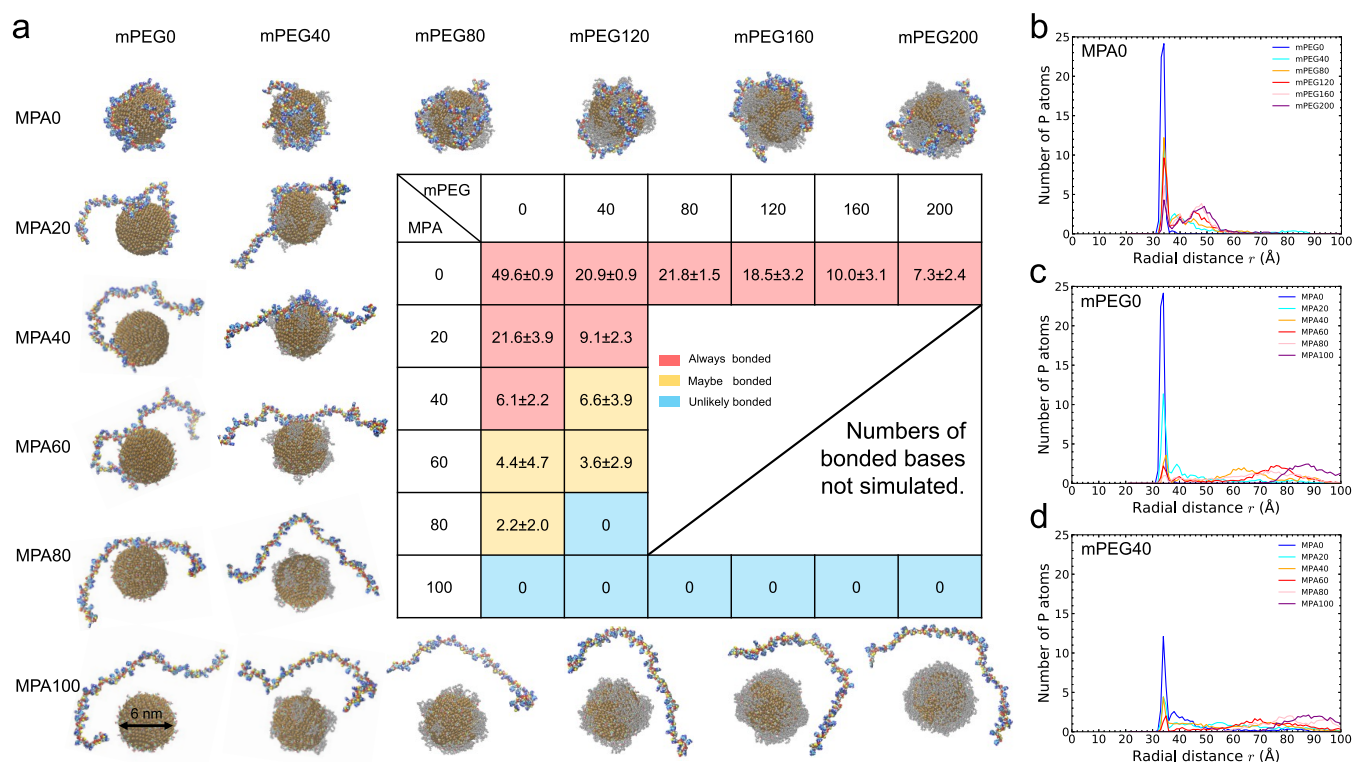
Figure 1. Representative structures of different lengths of polyA chains (N_S:N = 5:51−51:51) in implicit water solution (a) and on a ZnS plane (b). (c) Comparison of the R_g of polyA in 12.5 mM Na^+ solution between our MD and theoretical model predictions, and the experimental results of Doniach and co-workers.[38] (d) The surface area projected by the polyA chains onto the ZnS plane is reported as a function of the number of bases in the chains observed in MD simulations, leading to an observed surface area coverage (Zn on the top) equal to 0.76 ± 0.07 nm^2 per base.

AuNPs using monovalently wrapped ssDNA by engineering a ssDNA chain with multiple domains of poly(adenine) (polyA). However, the use of valence control in designing DNA linked NP assembly remains elusive because of the lack of a complete characterization of the atomistic structure of ssDNA on the NP surface. Nevertheless, the self-assembly of these particles was demonstrated by Farlow et al.,[24] when they found the presence of divalent QDs arising when N = 70 chains contained less than 50 phosphorothioate (PS) modified bases. It remains to be answered how many ssDNA strands, at different chain lengths, can wrap on QDs of varying sizes. The mechanism for the attachment of ssDNA to a QD has also yet to be fully determined. The wrapping of QDs by ssDNA appears to be strongly affected by the nature of the ligands on the QD surface. The electrostatic interaction between the polyelectrolyte and interface, for example, is critical to the structure of polyelectrolyte[25] and the self-assembly of proteins.[26,27] Negatively charged ligands, such as 3-mercaptopropionic acid (MPA), induce a strong electrostatic repulsion effect. Large or bulky ligands, such as O-(2-mercaptoethyl)-O'-methyl-hexa-(ethylene glycol) (mPEG), occupy a large surface space and induce a strong steric exclusion effect.[28] It remains a challenge to fully quantify the combination of both steric exclusion and electrostatic repulsion effects in relating the QD surface charge and ligand coverage to the resulting wrapping of a given QD by ssDNA.

There is precedence for the use of experimental and computational methods to reveal aspects of the atomistic structure of DNA on a QD. For example, Guo et al.[23] measured the distance from different locations on the ssDNA and dsDNA attached to a QD using Tb-DNA probes with FRET spectroscopy. They found that the conformation of a double-stranded DNA (dsDNA) is fully extended in the QD radial direction, and that, on the other hand, the ssDNA is in a flexible conformation wrapping the QD.[23] Using molecular dynamics (MD) simulations, Zhu et al.[29] reported the maximum number of ssDNA strands attached to a AuNP across a library of cases with varying polyA lengths (N = 10−40) and AuNP diameters (D = 5−50 nm). Their MD simulations suggested a connection between the valence number and AuNP diameter. They found, for example, that only 1 polyA (length N = 40) chain attaches to a 5 nm diameter AuNP, and 14 polyAs (length N = 40) attach to a 10 nm diameter AuNP.[29] However, the valence number computed in ref 29. is much higher than that found in the experimental results of refs 18, 24, and 30. This discrepancy is perhaps a consequence of the approximation used in ref 29. in interpreting their MD simulations through the effective contact area, as it is very much affected by the subtle balance between steric exclusion and electrostatic repulsion. Additional recent examples of the use of computational models to describe the binding of DNA to a surface include the calculation of the desorption energy of ssDNA on a gold surface,[31] the use of different force fields to model the attachment of ssDNA to a gold surface,[32] the modeling of ssDNA wrapping on a single-walled carbon naonotube (SWCNT),[33] and the determination of the entropic contribution to the attractive interaction between DNA linked NPs.[34]

In this work, we combine experiments and MD simulations to reveal the detailed mechanism and structure of ssDNA wrapping on a ZnS QD of different sizes at the atomistic scale. We have partially answered questions regarding the effects of

Figure 2. (a) Representative structures of ssDNA (polyA) with 51 PS-bases (N_S:N = 51:51) wrapping on a D = 6 nm QD capped with different numbers of MPA and mPEG. The table imbedded in panel a lists the average number of bonded bases (at distances ≤5 Å from the QD surface) calculated from 2 to 5 different structures in MD simulation. Boxes are colored based on our simulation observations: yellow refers to observation of both bonded and nonbonded structures, blue refers to observation of only all-nonbonded structures, and red refers to observation of only all-bonded structures. (b)−(d) Radial number distributions of P atoms (on the ssDNA backbone) near a D = 6 nm QD with different numbers of MPA and mPEG capping: (b) changing N(mPEG) from 0 to 200 with no MPA, (c) changing N(MPA) from 0 to 100 with no mPEG and (d) changing N(MPA) from 0 to 100 with N(mPEG) = 40 capping together.

the QD size, ligand capping, and valence number on the mechanism of ssDNA wrapping a QD. The conformations of ssDNA alone and on a ZnS plane found in our MD simulation model are validated by comparison to experimental and simulation results from the literature. We obtain the MPA and mPEG ligand capping effects on the wrapping of NPs by ssDNA, and find that they are affected by the electrostatic repulsion and steric hindrance effects as we anticipated from the discussion above. We focus on the structure of the wrapping of one ssDNA on QDs with varying size (D: 3, 6, 9, and 14 nm) and at different ratios (N_S/N) of PS modification. We use FRET experiments to demonstrate the QD size effect on the distance between the ssDNA head and QD surface. Finally, the ssDNA (length N = 51) valence numbers on different sizes of QDs (D: 6, 9, and 14 nm) are estimated using MD simulations and confirmed by comparison to the structure of QD assemblies obtained by transmission electron microscopy (TEM).

RESULTS AND DISCUSSION

Structure of ssDNA Alone and on a Flat ZnS Plane. Computational modeling[35,36] and experimental measurement[37−43] of DNA structure continues to be an active area of research because of the importance of DNA molecules to living systems. In our MD simulation model, we use the Consistent-Valence Force Field (CVFF)[44] to describe the interactions on an ssDNA chain (polyA of different lengths, N = 5−51). The water solvent is implicitly considered through a

dielectric constant set at 80. The assumption of implicit water is common in large-scale simulations because it speeds them up dramatically. Some of us found, for example, that such effects are small at the length scales of interest here in determining the ς-potential of AuNPs also modeled in this work.[45]

Each adenine base carries a charge of −1e that is neutralized with a counterion, Na⁺. Our model conditions correspond to a low salt concentration environment and no additional salt ions are needed or added to the system. Figure 1a,b show representative structures of polyA of different lengths alone and attached to the ZnS plane, respectively. From the self-avoiding walk (SAW) model, we expect the polyA radius of gyration to be $R_g = \frac{b}{\sqrt{6}}\left(\frac{aN}{b}\right)^v$,[35] where N is the number of bases, a is the effective monomer length, b is the Kuhn segment length, and v is the scaling exponent. As suggested by refs[35] and [38], we set the parameters either as a = 6.5 Å, b = 20 Å, and v = 0.588 corresponding to 1 M Na⁺ concentration, or as a = 6.5 Å, b = 30 Å, and v = 0.72 corresponding to 0.1 M Na⁺ concentration; see Figure 1c.[31,34] The R_g found in the MD simulations lie between the high salt and low salt model; see Figure 1c. Using explicit water MD simulations and experimental measurements, Corcelli and co-workers[46−48] found that the structures of DNA and the surrounding water are important to each other. In our simulations, the R_g values of a solvated polyA N30 found in the simulations using the implicit water model compare well with those found from the control simulations using an explicit TIP3P water model; see
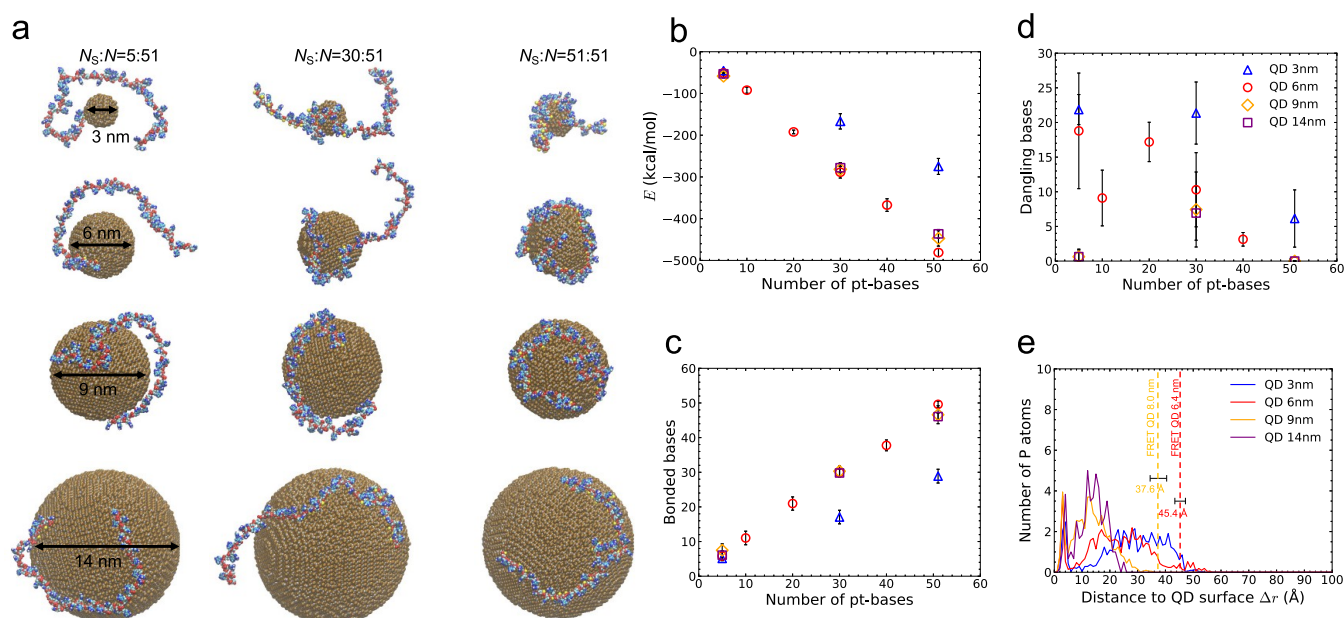
Figure 3. (a) Representative structures of ssDNA (polyA $N = 51$) on different sizes of QDs, with the number of PS-bases changes from $N_S = 5-51$ and QD size changes from $D = 3$ to 14 nm. Relationships of (b) interfacial binding energy between ssDNA and QD, (c) the number of bonded bases (at distances ≤ 5 Å from the QD surface), and (d) the number of dangling bases (at distances ≥ 30 Å from the QD surface) with the number of PS-bases and QD size. Panels b−e share the same legend. (e) MD results of radial number distribution of P atoms (on the ssDNA backbone) in polyA $N_S:N = 5:51$ wrapping different sizes of QDs (solid curves) and FRET experimental results of polyA $N_S:N = 5:51$ head to QD surface distances for $D = 6.4$ and 8 nm QDs (dashed lines). In panel e, radial distribution curves are shifted to the Δr axis with the origin set at the QD surface of the corresponding QD for comparison: $D = 3$ nm shifted by 15 Å, $D = 6$ nm shifted by 30 Å, $D = 9$ nm shifted by 45 Å, and $D = 14$ nm shifted by 70 Å.

Figure 1c. Equally importantly, the polyA R_g found in our MD model also agrees with the experimental measurements at low salt concentration of Doniach and co-workers;[38] see Figure 1c. For fixed total number N of bases equal to 51, we also find that changing the number of PS-bases (N_S from 5 to 51) does not affect the R_g of polyA, as reported in Figure S1 in the Supporting Information (SI).

The conformation of the solvated ssDNA changes upon binding to the QD surface. As a benchmark, we first consider the restructuring of ssDNA upon attachment to a flat ZnS plane; schemes are available in SI Figure S1. Following a similar approach, Fan and co-workers[32] used MD simulations to find that surface coverage area per base for polyA on a gold plane to be 0.7 ± 0.2 nm^2. In our work, we simulated five independent binding processes (five ensembles) of polyA on the ZnS plane; see Data 1−5 in Figure 1d. We find that the projection area (coverage) is linearly proportional to the number of bases. We found that the coverage area per base for polyA on ZnS plane is 0.76 ± 0.07 nm^2 which is quite similar to the earlier finding for a gold plane.[28] The structures of polyA attached to the ZnS plane with different lengths are shown in SI Figure S2. We also found that the R_g of polyA on the ZnS plane is slightly lower than polyA alone due to the binding interaction with the ZnS surface; see Figure 1c.

MPA and mPEG Capping Effect on ssDNA Wrapping QD. Negatively charged MPA ligands induce repulsion toward negatively charged ssDNA, ipso facto, and bulky mPEG ligands also induce steric exclusion toward the ssDNA wrapping on a QD.[28] The combination of these effects have led to the experimental observation that tuning the capping density of MPA and mPEG on the QD surface is critical to the ssDNA wrapping mechanism.[28] The effects of changing MPA and

mPEG surface capping densities on ssDNA wrapping a 6 nm diameter QD in our MD simulations are summarized in Figure 2. For quantitative analysis, we calculated the interfacial binding energy (E) between ssDNA and QD, R_g of the ssDNA, radial distribution of phosphorus atom numbers on the ssDNA backbone (to represent the ssDNA position), and the number of bonded (at distances ≤ 5 Å from the QD surface), dangling (at distances ≥ 30 Å from the QD surface) and middle ssDNA bases, which is available in SI Figure S3.

To uncover the mPEG capping effect, we vary the number of mPEG ligands for two cases: fixing the number of MPA ligands either at 0 or 100 (0 or 0.9 MPA/nm^2). The first row in Figure 2a shows that ssDNA can bind to the QD with $N(\text{MPA}) = 0$ regardless of the number of mPEG ligands, that is, as $N(\text{mPEG})$ varies from 0 to 200 (corresponding to 0−1.8 mPEG/nm^2 densities, and labeled mPEG0-mPEG100.) As $N(\text{mPEG})$ increases from 0 to 200, we find in Figure 2b, a decrease in the peaks at $r \sim 35$ Å, and an increase of ssDNA outside the QD to $r \sim 50$ Å. When $N(\text{mPEG})$ increases, the coverage of the QD surface by mPEG necessarily also increases. In turn, this reduces the binding sites available to ssDNA, viz the peak at ∼35 Å decreases, pushes more ssDNA bases away from the QD surface, and encourages the bases to stay next to the mPEG layer, viz the peak at ∼50 Å increases. This suggests that mPEG can block ssDNA through a steric exclusion effect. The number of bonded bases (at distances ≤ 5 Å from the QD surface) is summarized in the table imbedded in Figure 2a and also plotted in SI Figure S4. We found that at $N(\text{MPA}) = 0$, when the number of mPEG ligands increases, the interfacial binding energy increases and the R_g of ssDNA remains constant, which is reported in SI Figure S4. However, at $N(\text{MPA}) = 100$ (0.9 MPA/nm^2) when the number of
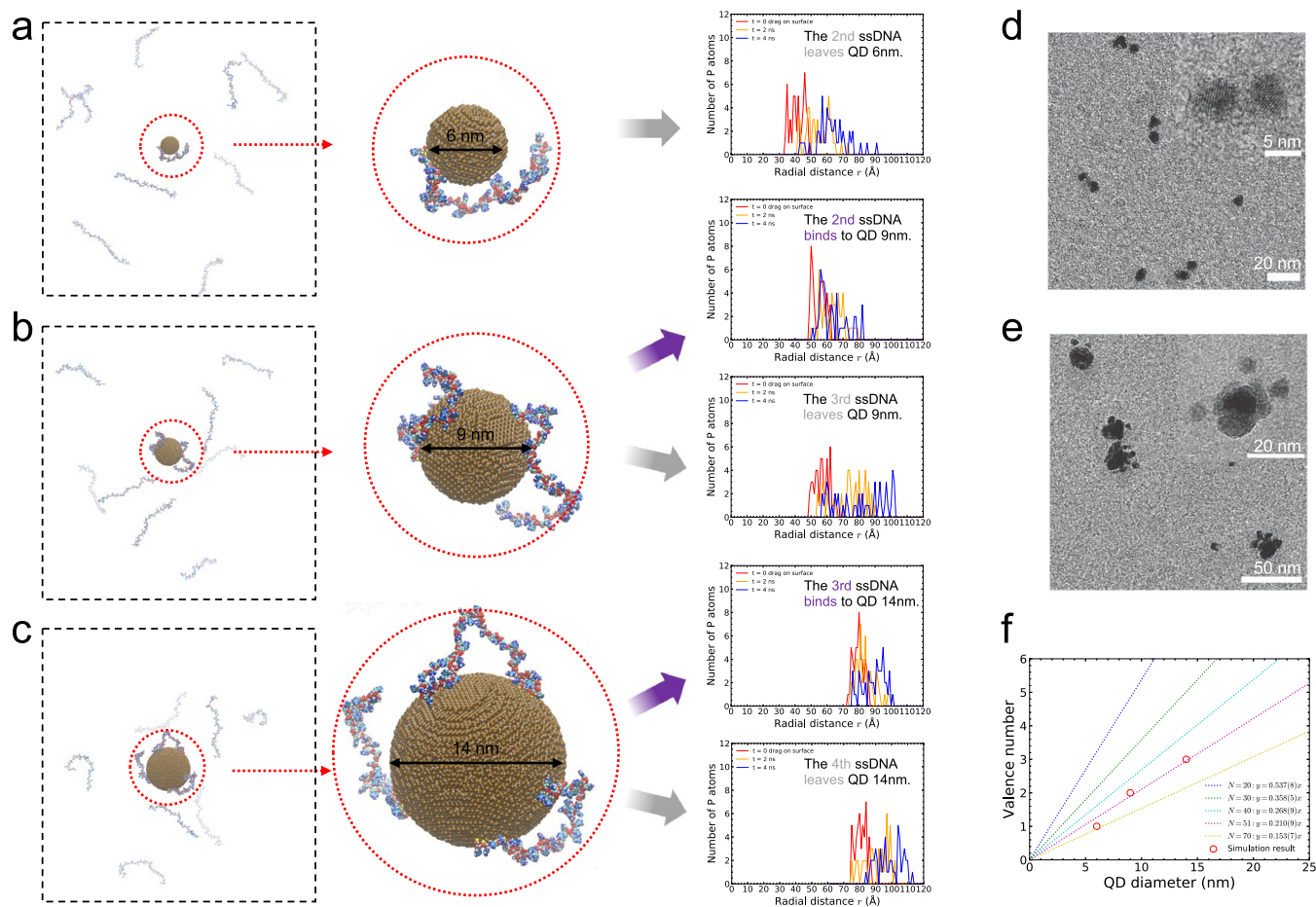
Figure 4. MD simulation demonstrations of (a) monovalence on D = 6 nm QD, (b) divalence on D = 9 nm QD, and (c) trivalence on D = 14 nm QD, using ssDNA polyA N_S:N = 5:51. TEM images with (d) dimers of two D = 6 nm QDs displaying monovalence, and (e) tetramers of one D = 14 nm QD linked with three D = 6 nm QDs displaying trivalent ssDNA on the 14 nm QD. (f) A linear relationship between ssDNA valence number and QD diameter using different lengths of ssDNA chains.

mPEG ligands increases, the ssDNA does not bind to the QD; see Figure 2a and SI Figure S4.

To understand the MPA capping effect, we once again address two cases, fixing the number of mPEG ligands either at 0 or 40, while changing the number of MPA ligands from 0 to 100 (and labeled MPA0-MPA100, respectively, in the table embedded in Figure 2a). We found that at constant N(mPEG) equal to 0 or 40, when the number of MPA ligands increases, the interfacial binding energy and the R_g of the ssDNA both increase, which is reported in SI Figure S4. For mPEG0—reported in column 1 in Figure 2a—we found both bonded and nonbonded structures (see the yellow zone) at MPA60 and MPA80. From MPA20 to MPA40, there is a significant drop in the number of bonded bases (21.6 to 6.1) as reported in the table in Figure 2a. Meanwhile, Figure 2c also shows a dramatic outside shift in the P atom number distribution at MPA40. This means that when N(MPA) ≥ 40, MPA can repel the ssDNA through electrostatic repulsion. In Figure 2c, we do not have any mPEG molecules on the QD and therefore *ipso facto* no electrostatic repulsion from them, and yet a similar structure emerges that necessarily arises from some consequence of the MPA. Because the MPA molecules are very small (see schemes in the first column of Figure 2a), the MPA molecules will not block the ssDNA through a steric exclusion mechanism. Thus, the shifts in the distributions in Figure 2c are induced by the electrostatic repulsion force arising from the

presence of MPA. A combination of both electrostatic repulsion and steric exclusion effects are reported in column 2 of Figure 2: At mPEG40, we found no bonded structures at MPA80 and the bonded structures appeared at MPA60. In comparison, at mPEG0, we found no bonded structures for MPA100, and bonded structures for MPA80. Due to the steric exclusion effect, the yellow zone is also shifted up at mPEG40. Figure 2d, and the table in Figure 2a reports that when MPA ≥ 20 and mPEG ≥ 40, the ssDNA is significantly repelled. To further demonstrate the combination of effects from MPA and mPEG capping, the phosphorus atom on each of the monomers can be used as a marker of the positions of the ssDNA monomers. The phosphorus (P) atom number distributions are compared for the attachment simulations for mPEG0 and mPEG40 at the same number of MPA ligands, which is available in SI Figure S5a-S,d in SI. SI Figures S5e,f confirm that ssDNA wrapping affinity on QDs can be enhanced by replacing MPA with mPEG while keeping the total number of ligands (MPA and mPEG) the same.

QD Size Effect on ssDNA Wrapping QD. The atomistic conformation of ssDNA wrapping NPs at varying sizes can reveal the possible structures resulting from the fabrication of functional NP assemblies. Figure 3a shows that for QDs ≥ 6 nm in diameter, all the PS-bases can bond to the QD surface. The interfacial binding energy and the number of bonded bases also show the same linear relationship with the number

of PS-bases, see Figure 3b,c. However, on the 3 nm diameter QD only part of the PS-bases can bond to the surface in the cases when the polyA PS-ratio N_S:N equals 30:51 or 51:51. It is generally true that for small QDs ($D = 3$ and 6 nm) and fixed N, the number of dangling bases ($\geq$30 Å away from the QD) increases with decreasing N_S in Figure 3d. However, $D = 9$ and 14 nm QDs have close to no dangling bonds, even at the low PS-ratio of 5:51. In order to keep the conformation energy of the ssDNA low, when the tail of the ssDNA is attached to the QD surface, the head of the ssDNA needs to leave the QD surface on small size QDs, but on large QDs it can stay near the QD surface; see Figure 3a. The R_g results are also available in SI Figure S7a.

The radial distributions of P atoms surrounding different sizes of QDs are compared in SI Figure S7c−f, for polyA N51 at different PS-base ratios from 5:51 to 51:51. Moreover, Figure 3e shows that for large QDs, $D = 9$ and 14 nm, all polyA bases with a 5:51 PS-base ratio stay near the QD surface (<30 Å), but for small QDs, $D = 3$ and 6 nm, some bases can reach out as far as 40−50 Å. Using FRET spectroscopy, we experimentally calculated the head to QD surface distance the 5:51 PS-ratio polyA, and found that the distance decreases from 45.4 to 37.6 Å when the QD size increases from $D = 6.4$ to 8 nm; see Figure 3e. Guo et al.[23] also found that the extension of ssDNA on the 9.2 nm diameter QD was ~1.5 Å per base using FRET spectroscopy, which gave a head to surface distance of 31.5 Å for 21 bases. This distance is reasonably shorter than our experimental result for the $D = 8$ nm QD, and it is in agreement with our simulation result for the $D = 9$ nm QD, wherein we see the head to surface distance to be ~ 30 Å. Our MD simulation and experimental work together confirm that the ssDNA chain stays closer to the QD surface when the QD size is larger. The photoluminescence spectra of the two QD-dye FRET systems are available in SI Figure S8.

Varying ssDNA Valence Number on Different Sizes of QDs. Considering only the steric exclusion effect, we find that the maximum number of ssDNA chains that can wrap on the QD is directly proportional to the QD surface area, $n = \frac{4\pi R^2}{NS_0}$, where n is the valence number, R is the QD radius, N is the number of bases on each ssDNA and S_0 is the surface coverage of each base. In this work, we found $S_0 = 0.76$ nm^2 for polyA with lengths $N = 51$, and maximum valence numbers $n = 3, 7$, and 16 on diameters of 6, 9, and 14 nm QDs, respectively, as recorded in SI Table S7. The drafted schemes of maximum ssDNA multivalence numbers on QDs 6, 9, and 14 nm are available in SI Figure S9. However, the actual valence number is much lower than the maximum number due to the electrostatic repulsion effect because the bonded ssDNA molecules can repel the approaching ssDNA. In our dilute salt model, sodium ions bind to an ssDNA rarely, and the effective charge carried by each ssDNA ($N = 51$) within typical interactions is ~50.

We find in our MD simulations that for the 6 nm QD, only monovalence is achievable. Attempts to attach a second ssDNA are spontaneously repelled; see Figure 4a. More detailed schemes and results indicating the lack of binding by a second ssDNA to the 6 nm QD may be found in SI Figures S10 and S11, where we provide three points of evidence to support the conclusion of monovalence: (1) The interfacial binding energy is near 0. (2) The distribution of the ssDNA (P atoms) moves away from the QD surface. The nonequilibrium

distributions of the ssDNA (P atoms) positions relative to nanoparticles with varying diameters are shown in the third column of Figure 4. Each of these plots shows the distribution at the specified time, and not the equilibrium distributions reported in Figure 2. (3) The number of bonded PS-bases ($\leq$5 Å) stays at 0 after 3 ns of simulation time. We also simulated polyA with different ratios of PS-bases, viz 5:51, 30:51, and 51:51 as reported in SI Figures S10 and S11, and the conclusions are the same.

For 9 nm QDs, we find that divalence is possible but trivalence was not observed; see Figure 4b for the divalent structure. SI Figures S12 and S13 also provide detailed schemes and results illustrating the binding of a second ssDNA to the 9 nm QD: (1) the interfacial binding energy is below 0; (2) the distribution of the ssDNA (P atoms) has a tail still attached to the QD surface; (3) the number of bonded bases ($\leq$5 Å) is above 0. Furthermore, SI Figures S14 and S15 show that a third ssDNA cannot bind to the 9 nm QD. Using similar methods, we find that for the 14 nm QD, trivalence is possible but tetravalence is not observed; see Figure 4c. The simulation schemes and calculation results for divalence, trivalence and tetravalence of 14 nm QDs with ssDNA are available in SI Figures S16−S21.

To demonstrate the valence number on different sizes of QDs, we conducted two physical experiments: (i) connecting the ssDNA wrapped 6 nm small QD with a complementary ssDNA wrapped 6 nm small QD; (ii) connecting the ssDNA wrapped 14 nm large QD with multiple complementary ssDNA wrapped 6 nm small QDs. The two QD-QD assemblies were prepared using the same DNA sequences, a hybridization part of 21 bases (with the complementary DNA), a wrapping part of 30 PS bases, 2 spacers, and 1 ending base adenine; see details on SI page S-5. The TEM image in Figure 4d suggests that experiment (i) can only lead to dimers and nonbonded QDs, which confirms monovalence on a 6 nm QD. The TEM image in Figure 4e suggests that tetramers are the most likely structures in experiment (ii), with one 14 nm QD connected to three 6 nm QDs. Although bonding to two or four 6 nm QDs is possible, it is very rare. This further suggests the trivalence of 14 nm QD by ssDNA structure according to experiment. It is notable that the experimental salt concentration (25 mM NaCl) is low enough that effects from the splitting of the salt can be ignored[45] in making comparison with the salt-less simulations of this work. Meanwhile in the experiment, the surface MPA molecules are mostly replaced by ssDNA monomers and neutralized by surface Na$^+$ counterions, and consequently the ssDNA−ssDNA interaction dominates the effects in agreement with the assumptions of the of our simulation model. The results may be sensitive to the nature of the ligand, and future work should characterize the growing family of larger and more complex ligands,[49] as for example, bidentate-zwitterionic ligands.[50]

From Gauss's law, the electric potential on the surface of a charged sphere is proportional to $\frac{Q}{R}$, where Q is the total charge on the sphere and R is the radius of the sphere. In our system, the repulsive electric potential of n ssDNA molecules on a QD induces an energy barrier (ΔE) that blocks the next ssDNA from bonding to the QD surface. In other words, the molecular diffusion (with thermal energy KE) cannot overcome this energy barrier for a certain valence number. At this critical point, $KE = \Delta E = \frac{Qq}{4\pi\varepsilon_0\varepsilon_r R}$, where q is the charge on

each ssDNA and $Q = nq$, n is the valence number, ε_0 is the vacuum permittivity, and ε_r is the dielectric constant of the medium. Given that the ssDNA chain length is fixed, ΔE and q are fixed, we can easily derive $n \propto R$. In turn, this means the maximum valence number is linearly proportional to the QD size (or diameter); see Figure 4f. We can also readily derive the related proportionality $n \propto \frac{R}{N}$, as shown in comparison with simulation in Figure 4f, for different lengths of ssDNA chains with different number of bases (N): As $KE \propto N$ and $q \propto N$, then $\frac{nN^2}{4\pi\varepsilon_0\varepsilon_r R} \propto \Delta E = KE \propto N$, and leading to $n \propto \frac{R}{N}$. This linear relationship is certainly surprising, and we look forward to further work verifying its applicability in a broader class of nanoparticles and ligands.

CONCLUSION

In this work, we use atomistic simulations and experiments to reveal the mechanism of ssDNA wrapping on a QD. Our ssDNA simulation model is validated using the R_g from the experimental measurement and the theoretical SAW model at low salt concentration region. We find that the surface coverage of PS-polyA on a flat ZnS plane is about 0.76 nm^2/base. Our simulation results show that MPA induces a steric exclusion effect and mPEG induces an electrostatic repulsion effect, and both prevent the ssDNA from binding to the QD surface. In order to wrap 6 nm QD with a ssDNA, the capping numbers should be approximately MPA ≤ 20 and mPEG ≤ 40. When the total number of capping ligand is fixed, N(MPA) + N(mPEG) is constant, replacing MPA with mPEG molecules can enhance ssDNA binding to the QD. We find in both our simulations and experiments that the ssDNA-QD structure is related to the QD size, and the ssDNA is closer to the QD surface when the QD size is larger. In the end, we found that the ssDNA valence number on a QD is primarily determined by the electrostatic repulsion effect, not the steric exclusion effect from the bonded ssDNA molecules. Using MD simulations of polyA with $N = 51$, we found a maximum number of 1, 2, and 3 ssDNA can bond to QDs with a diameter of 6, 9, and 14 nm, respectively. We confirmed the monovalence of 6 nm QD and trivalence of 14 nm QD structures using TEM images of QD-dimer and QD-tetramer assemblies, respectively. An implication of this electrostatic repulsion mechanism is the linear relation between the maximum valence number and the QD size, that is, $n \propto R$, observed in the simulations.

METHODS

MD Simulation Models and Methods. In this work, all MD simulations are propagated by the Large-scale Atomic Molecular Massive Parallel Simulator (LAMMPS) package.[51] The ssDNA model (polyA) is built using the BIOVIA Materials Studio (MS) software.[44] The Consistent-Valence Force Field (CVFF)[44,51] is used to describe the interactions, which is adopted from the MS software. The force field parameters are listed in SI Table S1–S6. The model for a given PS-base on the polyA chain is built by replacing an oxygen on the phosphate with a sulfur, available in SI Scheme S1. In general, the polyA chain has 51 repeating units ($N = 51$), of which we denote the number of unmodified bases as N_O and the number of PS-bases as N_S, such that $N = N_O + N_S$. The polyA is fully ionized, and each adenine unit carries -1 partial charge. Sodium ions (Na$^+$) are added to neutralize the total net charge. The radius of gyration (R_g) of our polyA simulation model is in good agreement with the literature.[35] The ZnS QDs of different sizes are built by LAMMPS. The ZnS Wurtzite crystal structure force field parameters are taken from ref 52.

The QD-ssDNA interfacial interaction Lennard-Jones (LJ) parameters (associated with Zn atoms) are set according to ref 53. The simulation box is $100 \times 100 \times 100$ nm^3. Water molecules are implicitly simulated by setting the dielectric constant to 80. The long-range Coulombic force is included by Ewald summation using the particle–particle particle-mesh (PPPM) algorithm in LAMMPS.[54]

MD Simulation Procedures. Multiple NVT (300 K) ensembles are used to relax the model and acquire results. Based on our previous experience in modeling cytochrome c interacting with a NP[55,56] and polymer wrapping on a NP,[57,58] we use the following seven steps to investigate the wrapping of QDs by ssDNA. (1) Initially, place ssDNA more than 10 nm away from the QD surface and relax the ssDNA chain and counterions (Na$^+$); (2) Steer the ssDNA to the QD surface, using a steering force 0.05 kcal/mol/Å toward the QD center, and setting the Zn−S (S on PS-polyA) LJ energy constant at 0.6 kcal/mol; (3) Uncoil the ssDNA chain conformation on the QD by relaxing the ssDNA with the Zn−S (S on PS-polyA) LJ energy constant 0.6 kcal/mol; (4) Steer the ssDNA to the QD surface again with a steering force 0.05 kcal/mol/Å toward the QD center, and increasing the Zn−S (S on PS-polyA) LJ energy constant to 3.0 kcal/mol; (5) Relax the ssDNA, using the Zn−S (S on PS-polyA) LJ energy constant 3.0 kcal/mol; (6) Attach the ssDNA to the QD surface by setting the Zn−S (S on PS-polyA) LJ energy constant to 10.0 kcal/mol; (7) After convergence, integrate the simulation and collect statistics using the Zn−S (S on PS-polyA) LJ energy constant 10.0 kcal/mol. The simulation time is 2−10 ns for each step. Typically, the final data is collected after convergence in 2 ns simulation time duration across 2−3 sample ensembles. More detailed information on our MD simulation implementation is provided in SI Section 1.

Experimental Materials. Quantum dots (QD600, QD630, and QD660), 3-mercaptopropionic acid (MPA), zinc acetate, O-(2-mercaptoethyl)-O′-methyl-hexa(ethylene glycol) (mPEG), trioctyl-phosphine oxide (TOPO), tetrabutylammonium bromide (TBAB) were all purchased from Sigma-Aldrich (details are available in SI). DNA oligonucleotides were all purchased from Integrated DNA Technologies (IDT; Coralville, IA) with standard desalting (for DNA oligonucleotides-without dye-modification) or HPLC (for dye-modified DNA oligonucleotides) as purification method. All ssDNA oligonucleotides were received as dry pellets.

Experimental Preparation of Aqueous QD with Neutral Surface Charge. Aqueous QD was prepared as described previously.[59] Briefly, 80 μL of QD (5 mg/mL) were incubated with TOPO (1 g/10 mL in chloroform) and chloroform at 25 °C and shacked. After 30 min, TBAB (0.3 M in chloroform) was added to this mixture. After additional 30 min incubation and shaking, Zn-MPA in NaOH solution was added. The mixture was vortexed and centrifuged with benchtop mini-centrifuge for 30 s, then the aqueous layer was recovered. These procedures were repeated until all aqueous layer were collected. MPA-QDs were purified to remove excess Zn-MPA and concentrated using ultra centrifugal filter for five times. After that, the MPA-QDs was diluted by adding 500 μL DNA free water and incubated with mPEG for 4 days at room temperature resulting in MPA/mPEG-QDs. The MPA/mPEG-QDs were again purified and concentrated using ultra centrifugal filter for five times. Moreover, the MPA/mPEG-QD buffer was exchanged into Tris using NAP-5 desalting column, preparing for DNA wrapping. The QD concentration was determined at 350 nm UV wavelength absorbance.[59]

Experimental Preparation of ssDNA Wrapped QD and QD-dye FRET Pairs. The ssDNA wrapped QD was also prepared as described previously.[59] Briefly, QD with neutral surface charge were incubated with PS-backbone modified ssDNA overnight for wrapping at a molar ratio of 1:10 (QD: ssDNA). After overnight incubation, the mixture was purified and concentrated using ultra centrifugal filter for five times. In the end, the QD concentration was measured again at 350 nm UV wavelength absorbance. To construct QD600-AF647 and QD630-AF647 pairs, the ssDNA wrapped QD600 and QD630 were incubated with dye (AF647) labeled complementary ssDNA. After reaction for 2 h, the fluorescence emission spectra of QD alone and

that with the presence of AF647 were recorded (details are available in SI).

Experimental Preparation of QD-QD Assembly. To make QD600-QD600 dimer assemblies (6−6 nm dimers), the ssDNA wrapped QD600 were mixed with the complementary ssDNA wrapped QD600 at a molar ratio of 5:1 (complementary ssDNA: ssDNA), at 25 mM NaCl and 10 mM Tris. To make QD660-QD600 (14−6 nm multivalence) assemblies, the ssDNA wrapped QD660 were mixed with the same complementary DNA wrapped QD600 at a molar ratio of 10:1 (complementary ssDNA: ssDNA), at 25 mM NaCl and 10 mM Tris. After overnight reaction, the mixture was drop-casted on 400 mesh carbon film square grids for transmission electron microscopy (TEM) imaging.

Experimental Measurement and FRET Calculation. Structural characterization of the QDs assemblies were carried out using a TEM at 120 kV. Absorbance spectra were measured using a UV−vis spectrophotometer (Thermo-Fisher) and the PL spectra were measured using a FluoroMax-4C (Horiba Jobin Yvon). The extinction coefficient of QD was estimated using the first extinction absorption peak and calculated according to the empirical formula from refs 59 and 60. The quantum yield of QD was determined using the relative quantum yield determination method with rhodamine 101 in spectroscopic-grade ethanol as standard in refs 59 and 61. The Förster distances and FRET efficiencies were calculated according to ref 62. (details are available in SI).

ASSOCIATED CONTENT

Ⓢ Supporting Information
The Supporting Information is available free of charge at https://pubs.acs.org/doi/10.1021/acsnano.2c01178.

> Detailed information for our methods and results. Tables S1−S6 and Scheme S1 provide MD force field parameters. Figures S1 and S2 provide ssDNA structures on a flat plane. Figures S3−S8 are about ssDNA wrapping QD, including ligand (MPA and mPEG) and capping QD size effects. Figure S9−S21 and Table S7 are about multivalence ssDNA on a QD (PDF)

AUTHOR INFORMATION

Corresponding Author
Rigoberto Hernandez − *Department of Chemistry, Chemical & Biomolecular Engineering, and Materials Science & Engineering, Johns Hopkins University, Baltimore, Maryland 21218, United States;* ⓘ orcid.org/0000-0001-8526-7414; Email: r.hernandez@jhu.edu

Authors
Xingfei Wei − *Department of Chemistry, Johns Hopkins University, Baltimore, Maryland 21218, United States;* ⓘ orcid.org/0000-0001-5924-1579

Chi Chen − *Department of Biological Engineering, Massachusetts Institute of Technology, Cambridge, Massachusetts 02139, United States;* ⓘ orcid.org/0000-0002-6126-1824

Yinong Zhao − *Chemical & Biomolecular Engineering, Johns Hopkins University, Baltimore, Maryland 21218, United States;* ⓘ orcid.org/0000-0002-7113-0481

Ewa Harazinska − *Department of Chemistry, Johns Hopkins University, Baltimore, Maryland 21218, United States;* ⓘ orcid.org/0000-0001-7139-3698

Mark Bathe − *Department of Biological Engineering, Massachusetts Institute of Technology, Cambridge, Massachusetts 02139, United States;* ⓘ orcid.org/0000-0002-6199-6855

Complete contact information is available at:

https://pubs.acs.org/10.1021/acsnano.2c01178

Notes
The authors declare no competing financial interest.

REFERENCES
(1) Bathe, M.; Hernandez, R.; Komiyama, T.; Machiraju, R.; Neogi, S. Autonomous Computing Materials. *ACS Nano* **2021**, *15*, 3586−3592.

(2) Jiang, S.; Zhang, F.; Yan, H. Complex Assemblies and Crystals Guided by DNA. *Nat. Mater.* **2020**, *19*, 694−700.

(3) Rogers, W. B.; Shih, W. M.; Manoharan, V. N. Using DNA to Program the Self-Assembly of Colloidal Nanoparticles and Microparticles. *Nat. Rev. Mater.* **2016**, *1*, 16008.

(4) Gang, O.; Tian, Y.; Kahn, J. S.; Xiong, Y.; Minevich, B.; Kumar, S. K. 3d-Organized Nanomaterials Through DNA-Prescribed and Valence-Controlled Material, U.S. Patent Application No. 17/070, 2021, 643.

(5) Tan, S. J.; Campolongo, M. J.; Luo, D.; Cheng, W. Building Plasmonic Nanostructures with DNA. *Nat. Nanotechnol.* **2011**, *6*, 268−276.

(6) Kim, T.; Nam, K.; Kim, Y. M.; Yang, K.; Roh, Y. H. DNA-Assisted Smart Nanocarriers: Progress, Challenges, and Opportunities. *ACS Nano* **2021**, *15*, 1942−1951.

(7) Veneziano, R.; Moyer, T. J.; Stone, M. B.; Wamhoff, E.; Read, B. J.; Mukherjee, S.; Shepherd, T. R.; Das, J.; Schief, W. R.; Irvine, D. J.; Bathe, M. Role of Nanoscale Antigen Organization on B-cell Activation Probed Using DNA Origami. *Nat. Nanotechnol.* **2020**, *15*, 716−723.

(8) Jones, M. R.; Seeman, N. C.; Mirkin, C. A. Programmable Materials and the Nature of the DNA Bond. *Science (American Association for the Advancement of Science)* **2015**, *347*, 1260901.

(9) Wang, S.; Lee, S.; Du, J. S.; Partridge, B. E.; Cheng, H. F.; Zhou, W.; Dravid, V. P.; Lee, B.; Glotzer, S. C.; Mirkin, C. A. The Emergence of Valency in Colloidal Crystals through Electron Equivalents. *Nat. Mater.* **2022**. DOI: 10.1038/s41563-021-01170-5.

(10) Murphy, C. J.; Vartanian, A. M.; Geiger, F. M.; Hamers, R. J.; Pedersen, J.; Cui, Q.; Haynes, C. L.; Carlson, E. E.; Hernandez, R.; Klaper, R. D.; Orr, G.; Rosenzweig, Z. Biological Responses to Engineered Nanomaterials: Needs for the Next Decade. *ACS Cent. Sci.* **2015**, *1*, 117−123.

(11) Chou, L. Y. T.; Zagorovsky, K.; Chan, W. C. W. DNA Assembly of Nanoparticle Superstructures for Controlled Biological Delivery and Elimination. *Nat. Nanotechnol.* **2014**, *9*, 148−155.

(12) Bhatia, D.; Arumugam, S.; Nasilowski, M.; Joshi, H.; Wunder, C.; Chambon, V.; Prakash, V.; Grazon, C.; Nadal, B.; Maiti, P. K.; Johannes, L.; Dubertret, B.; Krishnan, Y. Quantum Dot-Loaded Monofunctionalized DNA Icosahedra for Single-Particle Tracking of Endocytic Pathways. *Nat. Nanotechnol.* **2016**, *11*, 1112−1119.

(13) Freeman, R.; Finder, T.; Willner, I. Multiplexed Analysis of Hg2+ and Ag+ Ions by Nucleic Acid Functionalized CdSe/ZnS Quantum Dots and Their Use for Logic Gate Operations. *Angew. Chem., Int. Ed.* **2009**, *48*, 7818−7821.

(14) Kim, S.; Kim, N.; Seo, J.; Park, J.; Song, E. H.; Choi, S. Y.; Kim, J. E.; Cha, S.; Park, H. H.; Nam, J. Nanoparticle-Based Computing

Architecture for Nanoparticle Neural Networks. *Sci. Adv.* **2020**, *6*, No. eabb3348.

(15) Schreiber, R.; Santiago, I.; Ardavan, A.; Turberfield, A. J. Ordering Gold Nanoparticles with DNA Origami Nanoflowers. *ACS Nano* **2016**, *10*, 7303–7306.

(16) Lin, Z.; Xiong, Y.; Xiang, S.; Gang, O. Controllable Covalent-Bound Nanoarchitectures from DNA Frames. *J. Am. Chem. Soc.* **2019**, *141*, 6797–6801.

(17) Xiong, Y.; Yang, S.; Tian, Y.; Michelson, A.; Xiang, S.; Xin, H.; Gang, O. Three-Dimensional Patterning of Nanoparticles by Molecular Stamping. *ACS Nano* **2020**, *14*, 6823–6833.

(18) Yao, G.; Li, J.; Li, Q.; Chen, X.; Liu, X.; Wang, F.; Qu, Z.; Ge, Z.; Narayanan, R. P.; Williams, D.; Pei, H.; Zuo, X.; Wang, L.; Yan, H.; Feringa, B. L.; Fan, C. Programming Nanoparticle Valence Bonds with Single-Stranded DNA Encoders. *Nat. Mater.* **2020**, *19*, 781–788.

(19) Hastman, D. A.; Melinger, J. S.; Aragonés, G. L.; Cunningham, P. D.; Chiriboga, M.; Salvato, Z. J.; Salvato, T. M.; Brown, C. W.; Mathur, D.; Medintz, I. L.; Oh, E.; Díaz, S. A. Femtosecond Laser Pulse Excitation of DNA-Labeled Gold Nanoparticles: Establishing a Quantitative Local Nanothermometer for Biological Applications. *ACS Nano* **2020**, *14*, 8570–8583.

(20) Li, M.; Cushing, S. K.; Wang, Q.; Shi, X.; Hornak, L. A.; Hong, Z.; Wu, N. Size-Dependent Energy Transfer between CdSe/ZnS Quantum Dots and Gold Nanoparticles. *J. Phys. Chem. Lett.* **2011**, *2*, 2125–2129.

(21) Coopersmith, K.; Han, H.; Maye, M. M. Stepwise Assembly and Characterization of DNA Linked Two-Color Quantum Dot Clusters. *Langmuir* **2015**, *31*, 7463–7471.

(22) Pan, K.; Boulais, E.; Yang, L.; Bathe, M. Structure-Based Model for Light-Harvesting Properties of Nucleic Acid Nanostructures. *Nucleic Acids Res.* **2014**, *42*, 2159–2170.

(23) Guo, J.; Qiu, X.; Mingoes, C.; Deschamps, J. R.; Susumu, K.; Medintz, I. L.; Hildebrandt, N. Conformational Details of Quantum Dot-DNA Resolved by Förster Resonance Energy Transfer Lifetime Nanoruler. *ACS Nano* **2019**, *13*, 505–514.

(24) Farlow, J.; Seo, D.; Broaders, K. E.; Taylor, M. J.; Gartner, Z. J.; Jun, Y. Formation of Targeted Monovalent Quantum Dots by Steric Exclusion. *Nat. Methods* **2013**, *10*, 1203–1205.

(25) Troiano, J. M.; McGeachy, A. C.; Olenick, L. L.; Fang, D.; Liang, D.; Hong, J.; Kuech, T. R.; Caudill, E. R.; Pedersen, J. A.; Cui, Q.; Geiger, F. M. Quantifying the Electrostatics of Polycation–Lipid Bilayer Interactions. *J. Am. Chem. Soc.* **2017**, *139*, 5808–5816.

(26) McManus, J. J.; Charbonneau, P.; Zaccarelli, E.; Asherie, N. The Physics of Protein Self-Assembly. *Curr. Opin. Colloid Interface Sci.* **2016**, *22*, 73–79.

(27) Simon, A. J.; Zhou, Y.; Ramasubramani, V.; Glaser, J.; Pothukuchy, A.; Gollihar, J.; Gerberich, J. C.; Leggere, J. C.; Morrow, B. R.; Jung, C.; Glotzer, S. C.; Taylor, D. W.; Ellington, A. D. Supercharging Enables Organized Assembly of Synthetic Biomolecules. *Nat. Chem.* **2019**, *11*, 204–212.

(28) Shen, J.; Tang, Q.; Li, L.; Li, J.; Zuo, X.; Qu, X.; Pei, H.; Wang, L.; Fan, C. Valence-Engineering of Quantum Dots Using Programmable DNA Scaffolds. *Angew. Chem., Int. Ed.* **2017**, *56*, 16077–16081.

(29) Zhu, D.; Li, J.; Wang, L.; Li, Q.; Wang, L.; Song, B.; Zhou, R.; Fan, C. Hydrophobic Collapse-Driven Nanoparticle Coating With Poly-Adenine Adhesives. *Chem. Commun. (Cambridge, U. K.)* **2021**, *57*, 381–384.

(30) Zhang, T.; Liedl, T. DNA-Based Assembly of Quantum Dots Into Dimers and Helices. *Nanomaterials (Basel)* **2019**, *9*, 339.

(31) Rapino, S.; Zerbetto, F. Modeling the Stability and the Motion of DNA Nucleobases on the Gold Surface. *Langmuir* **2005**, *21*, 2512–2518.

(32) Jiang, X.; Gao, J.; Huynh, T.; Huai, P.; Fan, C.; Zhou, R.; Song, B. An Improved DNA Force Field for ssDNA Interactions with Gold Nanoparticles. *J. Chem. Phys.* **2014**, *140*, 234102.

(33) Ghosh, S.; Patel, N.; Chakrabarti, R. Probing the Salt Concentration Dependent Nucleobase Distribution in a Single-Stranded DNA–Single-Walled Carbon Nanotube Hybrid with Molecular Dynamics. *J. Phys. Chem. B* **2016**, *120*, 455–466.

(34) Sciortino, F.; Zhang, Y.; Gang, O.; Kumar, S. K. Combinatorial-Entropy-Driven Aggregation in DNA-Grafted Nanoparticles. *ACS Nano* **2020**, *14*, 5628–5635.

(35) Henrich, O.; Gutiérrez Fosado, Y. A.; Curk, T.; Ouldridge, T. E. Coarse-Grained Simulation of DNA Using LAMMPS. *Eur. Phys. J. E* **2018**, *41*, 1–16.

(36) Chakraborty, D.; Hori, N.; Thirumalai, D. Sequence-Dependent Three Interaction Site Model for Single- and Double-Stranded DNA. *J. Chem. Theory Comput.* **2018**, *14*, 3763–3779.

(37) Tinland, B.; Pluen, A.; Sturm, J.; Weill, G. Persistence Length of Single-Stranded DNA. *Macromolecules* **1997**, *30*, 5763–5765.

(38) Sim, A. Y. L.; Lipfert, J.; Herschlag, D.; Doniach, S. Salt dependence of the Radius of Gyration and Flexibility of Single-Stranded DNA in Solution Probed by Small-Angle X-Ray scattering. *Phys. Rev. E* **2012**, *86*, No. 021901.

(39) Chen, H.; Meisburger, S. P.; Pabit, S. A.; Sutton, J. L.; Webb, W. W.; Pollack, L. Ionic strength-dependent persistence lengths of single-stranded RNA and DNA. *Proc. Natl. Acad. Sci. U.S.A.* **2012**, *109*, 799–804.

(40) Meisburger, S. P.; Sutton, J. L.; Chen, H.; Pabit, S. A.; Kirmizialtin, S.; Elber, R.; Pollack, L. Polyelectrolyte Properties of Single Stranded DNA Measured Using SAXS and Single-Molecule FRET: Beyond the Wormlike Chain Model. *Biopolymers* **2013**, *99*, 1032–1045.

(41) Plumridge, A.; Meisburger, S. P.; Pollack, L. Visualizing Single-Stranded Nucleic Acids in Solution. *Nucleic Acids Res.* **2017**, *45*, No. e66.

(42) Plumridge, A.; Meisburger, S. P.; Andresen, K.; Pollack, L. The Impact of Base Stacking on the Conformations and Electrostatics of Single-Stranded DNA. *Nucleic Acids Res.* **2017**, *45*, 3932–3943.

(43) Roth, E.; Glick Azaria, A.; Girshevitz, O.; Bitler, A.; Garini, Y. Measuring the Conformation and Persistence Length of Single-Stranded DNA Using a DNA Origami Structure. *Nano Lett.* **2018**, *18*, 6703–6709.

(44) Materials Studio Software. *Dassault Systèmes BIOVIA, Materials Studio, Version 8*, Dassault Systèmes, San Diego, 2014.

(45) Wei, X.; Popov, A.; Hernandez, R. Electric Potential of Citrate-Capped Gold Nanoparticles Is Affected by Poly(allylamine hydrochloride) and Salt Concentration. *ACS Appl. Mater. Interfaces* **2022**, *14*, 12538.

(46) Furse, K. E.; Corcelli, S. A. The Dynamics of Water at DNA Interfaces: Computational Studies of Hoechst 33258 Bound to DNA. *J. Am. Chem. Soc.* **2008**, *130*, 13103–13109.

(47) Furse, K. E.; Corcelli, S. A. Molecular Dynamics Simulations of DNA Solvation Dynamics. *J. Phys. Chem. Lett.* **2010**, *1*, 1813–1820.

(48) McDermott, M. L.; Vanselous, H.; Corcelli, S. A.; Petersen, P. B. DNA's Chiral Spine of Hydration. *ACS Cent. Sci.* **2017**, *3*, 708–714.

(49) Banerjee, A.; Pons, T.; Lequeux, N.; Dubertret, B. Quantum Dots–DNA Bioconjugates: Synthesis to Applications. *Interface focus* **2016**, *6*, 20160064.

(50) Zhan, N.; Palui, G.; Safi, M.; Ji, X.; Mattoussi, H. Multidentate Zwitterionic Ligands Provide Compact and Highly Biocompatible Quantum Dots. *J. Am. Chem. Soc.* **2013**, *135*, 13786–13795.

(51) Plimpton, S. Fast Parallel Algorithms for Short-Range Molecular Dynamics. *J. Comput. Phys.* **1995**, *117*, 1–19.

(52) Grünwald, M.; Zayak, A.; Neaton, J. B.; Geissler, P. L.; Rabani, E. Transferable Pair Potentials for CdS and ZnS Crystals. *J. Chem. Phys.* **2012**, *136*, 234111.

(53) Zhang, H.; Chen, B.; Ren, Y.; Waychunas, G. A.; Banfield, J. F. Response of nanoparticle structure to different types of surface environments: Wide-Angle X-Ray Scattering and Molecular Dynamics Simulations. *Phys. Rev. B* **2010**, *81*, 125444.

(54) Hockney, R. W.; Eastwood, J. W. *Computer simulation using particles*; CRC Press: Boca Raton, FL, 1988.

(55) Tollefson, E. J.; Allen, C. R.; Chong, G.; Zhang, X.; Rozanov, N. D.; Bautista, A.; Cerda, J. J.; Pedersen, J. A.; Murphy, C. J.; Carlson, E. E.; Hernandez, R. Preferential Binding of Cytochrome c to Anionic Ligand-Coated Gold Nanoparticles: A Complementary

Computational and Experimental Approach. *ACS Nano* **2019**, *13*, 6856−6866.

(56) Daly, C. A.; Allen, C.; Rozanov, N.; Chong, G.; Melby, E. S.; Kuech, T. R.; Lohse, S. E.; Murphy, C. J.; Pedersen, J. A.; Hernandez, R. Surface Coating Structure and Its Interaction with Cytochrome c in EG6-Coated Nanoparticles Varies with Surface Curvature. *Langmuir* **2020**, *36*, 5030−5039.

(57) Chong, G.; Laudadio, E. D.; Wu, M.; Murphy, C. J.; Hamers, R. J.; Hernandez, R. Density, Structure, and Stability of Citrate3− and H2citrate− on Bare and Coated Gold Nanoparticles. *J. Phys. Chem. C* **2018**, *122*, 28393−28404.

(58) Chong, G.; Hernandez, R. Adsorption Dynamics and Structure of Polycations on Citrate-Coated Gold Nanoparticles. *J. Phys. Chem. C* **2018**, *122*, 19962−19969.

(59) Chen, C.; Wei, X.; Parsons, M. F.; Guo, J.; Banal, J. L.; Zhao, Y.; Scott, M. N.; Schlau-Cohen, G. S.; Hernandez, R.; Bathe, M. Nanoscale 3D Spatial Addressing and Valence Control of Quantum Dots using Wireframe DNA Origami. *submitted.*

(60) Yu, W. W.; Qu, L.; Guo, W.; Peng, X. Experimental Determination of the Extinction Coefficient of CdTe, CdSe, and CdS Nanocrystals. *Chem. Mater.* **2003**, *15*, 2854−2860.

(61) Würth, C.; Grabolle, M.; Pauli, J.; Spieles, M.; Resch-Genger, U. Relative and Absolute Determination of Fluorescence Quantum Yields of Transparent Samples. *Nat. Protoc.* **2013**, *8*, 1535−1550.

(62) Algar, W. R.; Hildebrandt, N.; Vogel, S. S.; Medintz, I. L. FRET as a Biomolecular Research Tool - Understanding Its Potential While Avoiding Pitfalls. *Nat. Methods* **2019**, *16*, 815−829.